Science Bulletin 64 (2019) 1152–1157

Contents lists available at ScienceDirect

Science Bulletin

journal homepage: www.elsevier.com/locate/scib

Article

Hollow nanostructure of sea-sponge-C/SiC@SiC/C for stable Li^+-storage capability

Weina Li [a,1], Jiaqi Li [a,1], Jiahao Wen [b], Ming Wen [a,*], Shipei Chen [a], Qingsheng Wu [a], Yongqing Fu [c]

[a] School of Chemical Science and Engineering, Shanghai Key Laboratory of Chemical Assessment and Sustainability, Tongji University, Shanghai 200092, China
[b] School of Electrical Engineering, Chongqing University, Chongqing 400044, China
[c] Faculty of Engineering and Environment, Northumbria University, NE1 8ST, UK

ARTICLE INFO

Article history:
Received 18 March 2019
Received in revised form 30 April 2019
Accepted 3 June 2019
Available online 14 June 2019

Keywords:
SiC
Lithium ion batteries
Cycling stability
Sea-sponge-C/SiC@SiC/C

ABSTRACT

For the purpose of stable performance in energy storage systems, a new hollow nanostructure of sea-sponge-C/SiC@SiC/C (SCS/SiC@SiC/C) has been successfully fabricated by the SCS/SiC nanospheres coated with SiC/C shells through an *in situ* reduction process. Based on SCSs and the carbon shells, the stable hollow structures of SCS/SiC@SiC/C can contain large proportion of active SiC layers, which are adhered to both SCSs and the inner surfaces of carbon shells. Such nanostructured anode enables an excellent cycling stability with a capacity of 612 mAh/g at a current density of 0.5 A/g after 1,800 cycles, achieving an excellent stable Li^+-storage capability.

1. Introduction

The ever-growing requirements for portable electronic devices have accelerated the development of lithium-ion batteries (LIBs) [1]. However, the mostly used anode material for the LIBs, e.g., graphite has a limited practical capacity of 372 mAh/g. Although some materials (e.g., Si) with large theoretical specific capacity were explored for the high energy density, there are still some problems including large volumetric expansion and low electrical conductivity [2–4]. To solve some of these problems, carbon is frequently introduced to fabricate a composite structure to achieve an improved cycling stability and excellent rate performance [5–10]. Silicon carbide (SiC), was previously considered as an inactive material, and only served to improve the structural stability [11]. However, several recent studies have reported the possibilities of the electrochemically lithiated SiC, which could be used as the electrode material for the LIBs. The chemical reactions of Li and SiC was detected when Li was deposited onto the SiC surface pre-coated by graphene [12]. The growth of graphene on SiC can increase the Li^+-storage capacity of SiC up to a value which is the double value of the graphite [13]. A bowl-like SiC nanostructure with ultra-thin SiC nanoshells encapsulated in hollow graphitic carbon spheres as the LIB anodes displayed unexpectedly high electrochemical performance [14].

However, low electrical conductivity and Li^+ diffusion are still critical issues for the SiC anode materials. Herein, we have proposed hollow nanospheres of sea-sponge-C/SiC@SiC/C (SCS/SiC@SiC/C) for the excellent Li^+-storage capability. Such the new design has the following advantages: (1) the stable nanostructure contains numerous inner interconnected-channels, not only can withstand large stresses caused by the volume changes of SiC, but also is beneficial for infiltration of the electrolyte and Li^+ diffusion; (2) besides improve the conductivity, the SCSs also contribute the growth of an intimately contacted SiC layer on surface, meanwhile the diffusion passway of Li^+ is greatly shortened; (3) owing to the lower volume expansion compare to Si, SiC could avoid the drawback of volume expansion/contraction in repeated cycling, pulverization and loss of electronic contact. Furthermore, the stable SiC can work as a scaffold to withstand the stresses induced from volume changes for the formation of a stable SEI, which may contribute to superior cycling stability; (4) the cycling performance of the SCS/SiC@SiC/C composite can be effectively improved compare to those of the SCS/SiC nanospheres, because the SiC/C shells can contribute to the increase of capacity and help to prevent the side reactions during charge/discharge processes.

In this work, the hollow nanostructure of SCS/SiC@SiC/C was successfully synthesized through an *in situ* reduction process [15]. It can exhibit excellent cycling stability when used as the anode material in LIBs. The results show that the capacity keeps

* Corresponding author.
E-mail address: m_wen@tongji.edu.cn (M. Wen).
[1] These authors contributed equally to this work.

https://doi.org/10.1016/j.scib.2019.06.014
2095-9273/

increasing after initial 60 cycles, and reach a value of 612 mAh/g after 1,800 cycles at 0.5 A/g. Its exceptionally long cycle stability is due to the formation of stable structures of interconnected SCS/SiC mesoporous spheres coated with SiC/C.

2. Experimental

2.1. Preparation of SCS/SiC@SiC/C composites

Based on previously reported work of SCSs synthesis [16,17], the SCS/SiO_2 spheres were prepared using a modified Stöber's method [18]. Typically, the SCS (30 mg) was dispersed in ethanol solution and ultrasonicated for 15 min. Cetyltrimethylammonium bromide (CTAB) solution (1.0 mL, 10 mmol/L) was added in the above solution under stirring. Then tetraethoxysilane (TEOS, 1.0 mL) and aqueous ammonia solution (1.0 mL) were sequentially added and continuously stirred for 1.0 h. The product was collected by centrifugation and washed with water and ethanol. Then the prepared SCS/SiO_2 (80 mg) was dissolved into ethanol with CTAB solution (1.0 mL, 10 mmol/L), and stirred for 20 min. Then aqueous ammonia (0.3 mL) and 50 mg resorcinol were added into the above solution to stir 30 min, formaldehyde solution (0.1 mL) was added to kept for 2.0 h. The products were collected by centrifugation, washed by water and ethanol. The as-prepared powders were then transferred into a tubular furnace and heated at 800 °C under Ar for 2.0 h. The obtained SCS/SiO_2 or SCS/SiO_2@C samples were mixed with Mg powder in a molar ratio of 1:2, and then heated to 800 °C with a heating rate of 20 °C/min in a tube furnace under Ar for 2 h. The resultant products were then carefully dispersed in a 0.5 mol/L HCl solution under stirring for 2 h and dispersed in 1% HF aqueous solution for 30 min to remove the byproducts and impurities. The final object products of SCS/SiC and SCS/SiC@SiC/C were washed with the deionized water for three times and dried at 70 °C in a vacuum oven for 24 h.

2.2. Characterizations

Morphologies and structures of the samples were characterized using a field emission scanning electron microscope (FE-SEM, JEOL, S-4800), a high resolution transmission electron microscope (HR-TEM, JEOL, JEM-2100EX) with selective area electron diffraction (SAED), X-ray diffraction (XRD, Bruker, D8 Advance) with Cu Kα radiation (λ = 0.154056 nm). Elemental mapping was carried out on energy disperse X-ray spectroscopy (EDS, Oxford, TN-5400). The molecular structure was characterized by Fourier transform infrared spectroscopy (FT-IR, Thermo, NEXUS), Raman spectra (Renishaw, inVia). The chemical bond information was analyzed by X-ray photoelectron spectroscope (XPS, Perkin Elmer, PHI-5000C ESCA) with Mg Kα radiation. Binding energy of the elements was calibrated using the containment carbon (C 1s = 284.6 eV) and analyzed using the XPS Peak 41. Weight loss was measured on thermo gravimetric analyzer (TGA, Netzsch, STA409PC). The specific surface area was investigated by adsorption isotherm of nitrogen (Micrometrics, ASAP2020), using the Brunauer-Emmett-Teller (BET) method.

2.3. Electrochemical measurements

Electrochemical measurements were performed using CR2016 coin-type cells assembled in an argon-filled glove box. To prepare the working electrodes, active materials were mixed with conductive carbon black and polyvinylidene fluoride (PVDF) binder (dissolved in *N*-methyl pyrrolidone) with a mass ratio of 7:2:1, the resulting slurry was uniformly casted onto a copper foil and dried overnight in a vacuum oven at 100 °C. Subsequently, the coated copper foil was punched into wafers with a diameter of 15 mm. The mass loading of the electrode was 1.5 ± 0.1 mg/cm^2. Then the coin cells were assembled with active materials as the anode, metallic lithium foil as the cathode, and glass fiber as separator. The electrolyte was a solution of $LiPF_6$ dissolved in mixed solvent of ethylene carbonate (EC) and dimethyl carbonate (DMC) (1:1 by volume). Galvanostatic electrochemical experiments were conducted using a multichannel battery test system (LAND CT2000A) at 25 °C. Cyclic voltammetry (CV, 0.1 mV/s) and electrochemical impedance spectroscopy (EIS, 100 kHz – 0.01 Hz, 10 mV) measurements were conducted using an electrochemical workstation (Princeton Applied Research Versa STAT4). The specific capacities of all the samples were calculated based on the total mass of active materials.

3. Results and discussion

Fig. 1a presents a schematic illustration of fabrication processes of the SCS/SiC@SiC/C nanocomposite based on SCSs (Fig. S1a online). Firstly, SCS/SiO_2 (Fig. S1b online) was prepared by evenly dispersing a layer of SiO_2 onto SCSs. Then, SCS/SiO_2 was encapsulated in a carbon layer to form SCS/SiO_2@C (Fig. S1c online) by coating a layer of resorcinol–formaldehyde shell which was transformed to carbon in the carbonization process at 800 °C for 3 h. With the assistance of Mg (which has a boiling point of =~650 °C) during the magnesiothermic reduction reaction, the layer of SiO_2 in SCS/SiO_2 reacted with SCS to produce SiC, while SiO_2 could react with both the inner SCS and the carbon shell in SCS/SiO_2@C. According to the following reactions [19]:

$$SiO_2 + 2Mg \rightarrow Si + 2MgO \quad (1)$$

$$SiO_2 + 2Mg + C \rightarrow SiC + 2MgO \quad (2)$$

The kinetics behind magnesiothermic reduction process were previously investigated for the production of both Si [20] and SiC [21–23] as anode of LIBs. It is believed that the SiO_2 is reduced to Mg_2Si which is then served as the intermediates and will form SiC when the Mg_2Si encounters carbon through a solid state diffusion [24]. Larger contact area between SiO_2 and C, higher heating rate and higher reaction temperature are favorable for the formation of SiC. The mechanism is shown in the inset of Fig. 1b. During the reduction process, all the parameters were carefully controlled to facilitate the formation of cubic SiC while to avoid the formation of Si. These parameters include: a high molar ratio of Mg:SCS/SiO_2@C of 2:1, a fast heating rate of 20 °C/min, a higher reaction temperature of 800 °C. Finally, a mixture of SCS/SiC or SCS/SiC@SiC/C, magnesium oxide and residual silica were obtained. Magnesium oxide and the remaining silica were completely washed away by the HCl and HF diluted aqueous solutions.

From the SEM and TEM images of SCS/SiC in Fig. 1d–f, the layer of SiC is well-distributed on the surface of SCSs and has a good contact among each other. Such a structure has a lot of inner spaces to allow the volume changes of active material for lithiation/delithiation processes. The *in situ* growth of the SiC layer ensures its good contact with SCSs, and enable SCS/SiC to perfectly remain in the sea-sponge-shapes (Fig. S1d online). The XRD pattern of the SCS/SiC shows several diffraction peaks at 2θ = 35.6°, 60.0°, 71.8°, which are identified as those from the cubic(β)-SiC phase (JCPDS No. 29-1129) (Fig. 1i (top)). The formation of crystalline SiC layer can be proved by the HR-TEM image and the corresponding SAED patterns. The lattice constant obtained from the HR-TEM image is 0.25 nm, which is the same with the (1 1 1) lattice face of a cubic SiC (Fig. 1g), and confirmed by the SAED pattern (Fig. 1h). EDS analysis (Fig. 1i (bottom)) reveals that the sample is composed of only silicon and carbon. It should be noted that there isn't any Mg

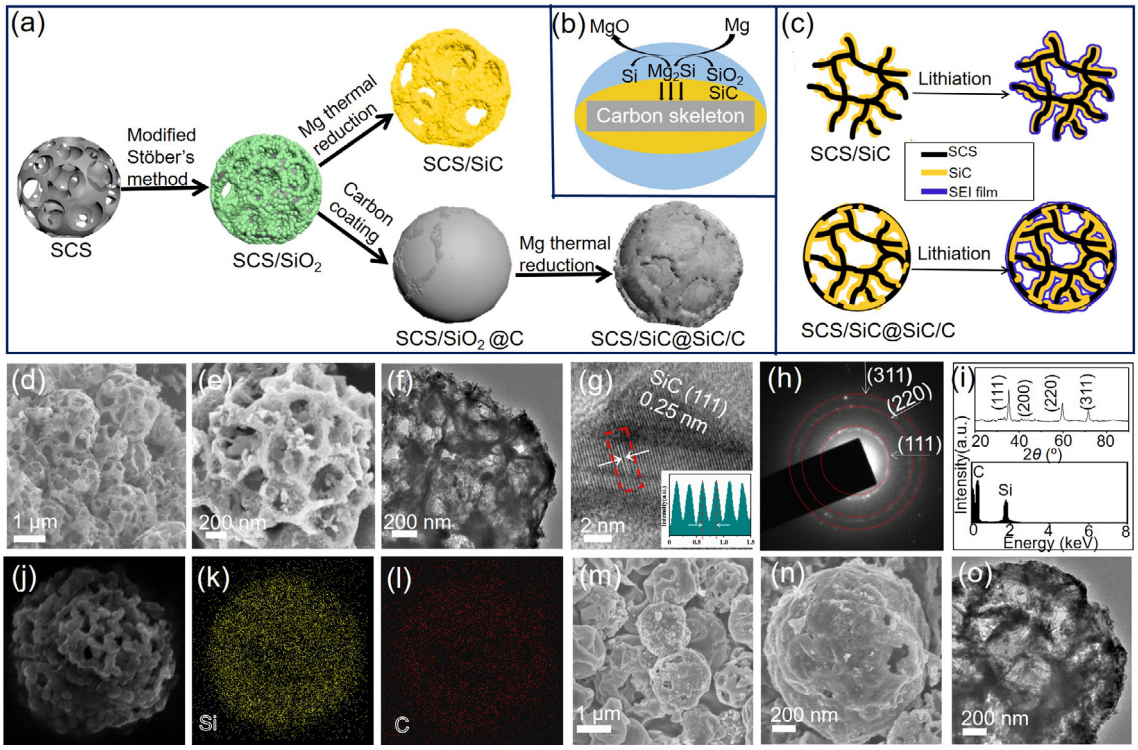

Fig. 1. (Color online) (a) The fabrication scheme of SCS/SiC@SiC/C nanospheres. (b) SiC formed by magnesiothermic reduction. (c) 2D cross-section view of the lithiation and delithiation process. (d)–(l) SEM, TEM, HRTEM images with inset crystal lattice spacing, SAED, XRD, EDS, Elemental mapping images of SCS/SiC spheres. (m)–(o) SEM and TEM images of SCS/SiC@SiC/C spheres.

(or magnesium oxide) signal detected, indicating the by-products of MgO formed in the magnesiothemic reduction process was successfully removed. Fig. 1j–l shows the comprehensive mapping image for C and Si elements overlapped with corresponding SEM image of SCS/SiC sample. The individual mappings of Si and C indicate the uniform distribution of SiC on the SCSs. Fig. 1m–o shows the SEM and TEM images of the SCS/SiC@SiC/C nanocomposite, which have an ordered inner hollow spherical structure with diameters ranging from 0.8 to 2.2 μm. Both of them retain the morphology of the SCSs without apparent changes even after the magnesiothermic reduction process and treatment with HCl and HF solutions. Such nanostructures can increase the chance of forming the electrochemically active SiC layer through increasing the contact areas with C to ensure a good electronic conductivity, which could enable the long-cycle stability for the Li^+-storage capability.

The successful etching of remained SiO_2 was also proved by checking the FT-IR spectra of SCS/SiC@SiC/C before and after the HF treatment. In the FT-IR spectra (Fig. 2a), two vibration peaks at 475 and 1,111 cm^{-1} assigned to Si—O bonds disappear after the remaining SiO_2 was removed [25]. Raman spectra shown in Fig. 2b, illustrate that the D band (electron decoherence in optics and transport phenomena in sp^2 carbons) and G band (E_{2g} mode of carbon) were observed at 1,322 and 1,594 cm^{-1}, respectively. The two more peaks at 780 and 940 cm^{-1} could be assigned to the transverse optical and longitudinal optical of SiC [26], indicating that SCS/SiC and SCS/SiC@SiC/C inherit the highly ordered backbone of the SCS and the ratio of I_D/I_G is increased due to the formation of more defects on the carbon layer. Fig. 2c shows the TG analysis. It's surprisingly to notice that, unlike SCS/SiC, the weight losses of SCS/SiC@SiC/C, i.e., the burning of carbon, can be divided into two stages, suggesting that there are two different types of carbon materials in the materials, e.g., the inner carbon backbone and the exterior carbon shell. Results show that the free carbon content is 26.6 wt% for SCS/SiC and 39.3 wt% for SCS/SiC@SiC/C. So both the samples are composites consisting of crystalline SiC and carbon with the mass ratio of SiC is 73.4 wt% in SCS/SiC and 60.9 wt% in SCS/SiC@SiC/C, respectively. XPS spectra (Fig. 2d) presents several peaks observed at around 95.5, 151.9, 285.2, 530.0 eV, which can be assigned to Si 2p, Si 2s, C 1s and O 1s, respectively. The survey spectra of SCS/SiC@SiC/C is similar to that of SCS/SiC due to same composition except that the C 1s peak in former is much higher than that of the later, indicating the formation of C shell. The detailed C 1s peak of SCS/SiC and SCS/SiC@SiC/C are displayed in Fig. 2e, f. The C 1s spectrum of SCS/SiC@SiC/C (Fig. 2f) can be fitted into several peaks which can be ascribed to C=O, carbide bonds from SiC and the different components of carbon bonds, respectively.

The electrochemical performances were evaluated and shown in Fig. 3. The CVs of SCS/SiC (Fig. 3a) and SCS/SiC@SiC/C (Fig. 3d) anodes for the initial 3 cycles with the potentials ranging from 0.05 to 3 V versus Li/Li^+, which display similar profiles of the lithiation and delithiation processes of SiC. Specifically, there are two humps that are appeared at around 1.0 and 0.7 V in the first reduction process but then disappeared in the next two cycles. This indicates the irreversible reaction as a result of the formation of SEI layer [27]. On the other hand, in the anodic side, the two peaks at about 0.15 and 0.2 V are attributed to the partly reversible delithiation process of SiC [28]. Meanwhile, Fig. 3b and e shows the galvanostatic charge/discharge profiles with different cycles at 0.5 A/g for SCS/SiC and SCS/SiC@SiC/C, respectively. There are a couple of slopes instead of the large plateaus of voltage during the first discharge process, which is different from those profiles of silicon but consistent with the previous reports that the fully lithiation of SiC produces Li_xSiC instead of Li_xSi. The cross-section view of the lithiation process for SCS/SiC and SCS/SiC@SiC/C are depicted in Fig. 1c. The impedance values and Nyquist plots of the electrodes are shown in Fig. 3c and f, respectively. The semicircles that correspond to the charge transfer resistances suggest

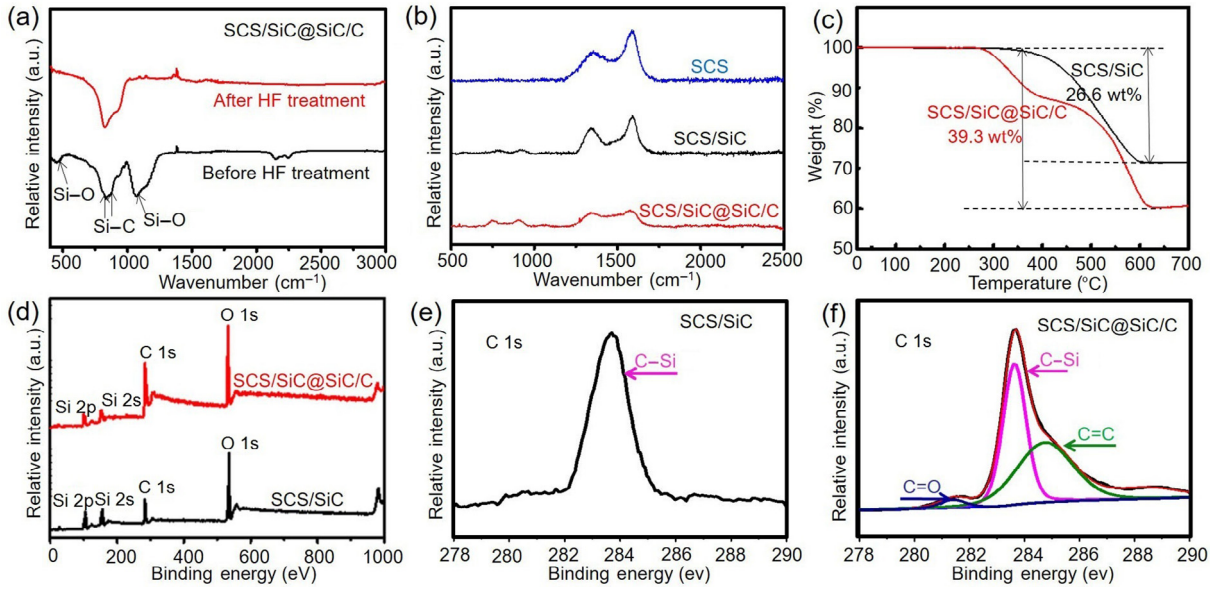

Fig. 2. (Color online) FT-IR spectra (a), Raman spectra (b), TG analysis (c), XPS full spectra (d), detail analysis of C 1s for SCS/SiC (e) and SCS/SiC@SiC/C (f).

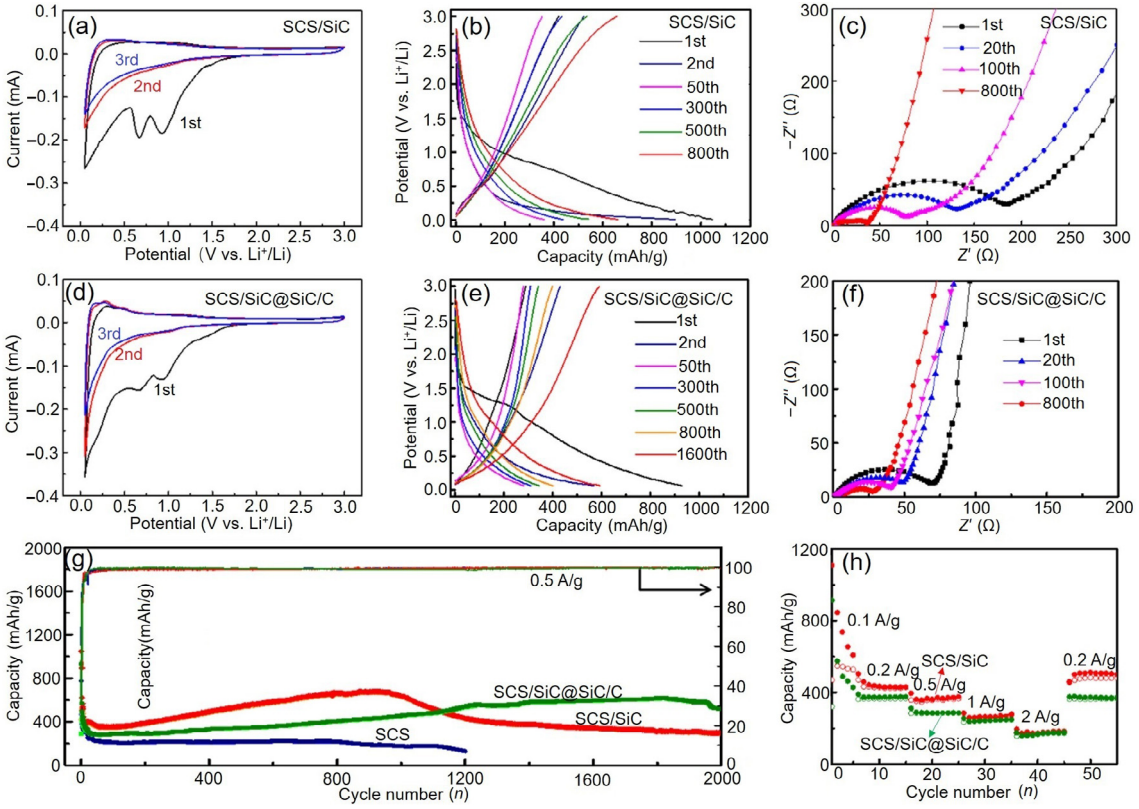

Fig. 3. (Color online) (a), (d) Cyclic voltammograms at a scan rate of 0.1 mV/s. (b), (e) Discharge-charge potential profiles at 0.5 A/g. (c), (f) Nyquist curves. (g) Cycling performances. (h) The rate performances.

that the impedance of the SCS/SiC@SiC/C is effectively decreased compared to that of the SCS/SiC due to the carbon shell. On the other hand, the repeated cycling can result in an improved conductivity for both of the electrode materials which suggests a better charge transport after a long-term cycling, and this is consistent with the increasing in capacity that was observed in Fig. 3g. Fig. 3g illustrates the long-term cycling stability of SCS/SiC and SCS/SiC@SiC/C composites at 0.5 A/g under the voltage window of 0.01–2.5 V. The cycling performance of the SCSs is also shown in the same figure for comparison. The SCS/SiC achieved an initial discharge capacity of 1,046.7 mAh/g. Then the capacity was declined until 60 cycles when a minimum value of 352 mAh/g was retained, and after that, the discharge capacity was increased steadily and gained a relatively high capacity of 662 mAh/g after 950 cycles. Fig. S2a (online) presents the cycling behavior of SCS/SiC. The continuously increased capacity is due to the activation

process of SiC and the enlarged surface areas caused by microstructural changes during the lithiation/delithiation, which offering more attachment sites and shortened transmission paths for Li^+. The initial discharge and charge capacities of SCS/SiC@SiC/C are 929.8 and 288.5 mAh/g (Fig. 3g), respectively, which are slightly lower than those of the SCS/SiC. It can be explained from the higher weight percentage of C in the SCS/SiC@SiC/C sample compared to that in the SCS/SiC, and such amorphous C exhibits less electrochemical activity than SiC. The Coulombic efficiency in the first-cycle was relatively low because the irreversible formation of SEI generated at the carbon layer surface, which consumes more lithium. The profile of cycling performance for SCS/SiC@SiC/C, although resembling that for SCS/SiC, suffers from fast decay in the first 60 cycles. However, it shows a continuously increasing tendency up to almost 2,000 cycles with a capacity value reaching 612 mAh/g. Table S1 (online) clearly demonstrates that the performance of SCS/SiC@SiC/C is more stable than those of the reported materials [22,23,27–29]. The structure of SCS/SiC@SiC/C can be well maintained after the long-term cycling (Fig. S2b online). These results suggested the exceptional structural durability and therefore excellent cycling stability of the SCS/SiC@SiC/C. The rate capabilities were evaluated at various current densities from 0.2 to 2 A/g and shown in Fig. 3h. Both the SCS/SiC and SCS/SiC@SiC/C nanocomposites can deliver stable capacities and then change to a higher capacity when the current density was reverted to 0.2 A/g, suggesting excellent rating performance and structural stability. It is also worthwhile to note that when the current density is increased to 1 and 2 A/g, the SCS/SiC@SiC/C delivered almost the same capacity compared to that of the SCS/SiC. However, the capacity of SCS/SiC@SiC/C is lower than those of SCS/SiC at 0.2 and 0.5 A/g. When the current density was switched back to 0.2 A/g at the 45th cycle again, the SCS/SiC could deliver a capacity of 480 mAh/g which is even higher than that achieved in the previous cycles. It might be that the high rate lithiation-induced reconstruction process is favorable for a stable SEI layer formation [30]. All the above results demonstrate that the as-obtained hollow nanostructure of SCS/SiC@SiC/C can achieve a good stability for nanostructures and long term cyclability for the LIBs applications.

4. Conclusions

In conclusion, the *in situ* magnesiothermic reduction process was carried out to synthesize the new hollow nanostructures of SCS/SiC@SiC/C. The unique architectural advantages combine the conductive SCSs and the mechanically stable hollow structures, the SCS/SiC@SiC/C anode material could enable excellent double stability for rate and cycling in LIBs, suggesting its great potential for electrochemical energy storage and conversion applications.

Conflict of interest

The authors declare that they have no conflict of interest.

Acknowledgments

This work was supported by the National Natural Science Foundation of China (21771140 and 51771138) and UK Engineering and Physical Sciences Research Council (EPSRC, EP/P018998/1).

Author contributions

Weina Li and Jiaqi Li contributed to the materials fabrication, characterization, and the electrochemical measurements. Jiahao Wen and Shipei Chen contributed to the data analysis. Ming Wen, Qingsheng Wu and Yongqing Fu contributed to manuscript writing.

Appendix A. Supplementary data

Supplementary data to this article can be found online at https://doi.org/10.1016/j.scib.2019.06.014.

References

[1] Armand M, Tarascon JM. Building better batteries. Nature 2008;451:652–7.
[2] McDowell MT, Lee SW, Cui Y, et al. Understanding the lithiation of silicon and other alloying anodes for lithium-ion batteries. Adv Mater 2013;25:4966–85.
[3] Kong XZ, Zheng YC, Wang YP, et al. Necklace-like Si@C nanofibers as robust anode materials for high performance lithium ion batteries. Sci Bull 2019;64:261–9.
[4] Liu N, Lu Z, Zhao J, et al. A pomegranate-inspired nanoscale design for large volume-change lithium battery anodes. Nat Nanotechnol 2014;9:187–92.
[5] Sun BL, Wen M, Wu QS, et al. Oriented growth & assembly of Ag@C@Co pentagonal prism nanocables and their highly activity selected catalysis along the edges for dehydrogenation. Adv Funct Mater 2012;22:2860–6.
[6] Zhang R, Du Y, Li D, et al. Highly reversible and large lithium storage in mesoporous Si/C nanocomposite anodes with silicon nanoparticles embedded in a carbon framework. Adv Mater 2014;26:6749–55.
[7] Fang H, Yang JH, Wen M, et al. Nanoalloy materials for chemical catalysis. Adv Mater 2018;30:1705698.
[8] Qin RH, Shao GQ, Hou JX, et al. One-pot synthesis of Li_3VO_4@C nanofibers by electrospinning with enhanced electrochemical performance for lithium-ion batteries. Sci Bull 2017;62:1081–8.
[9] Yan WX, Wu QN, Wen M, et al. A superior sodium/lithium-ion storage material: sea-sponge-C/Sn_2Fe@GO. Inorg Chem, 2019, doi: 10.1021/acs.inorgchem.9b00621.
[10] Lu Z, Liu N, Lee H, et al. Nonfilling carbon coating of porous silicon micrometer-sized particles for high-performance lithium battery anodes. ACS Nano 2015;9:2540–7.
[11] Chen Z, Zhou M, Cao Y, et al. In situ generation of few-layer graphene coatings on SnO_2-SiC core-shell nanoparticles for high-performance lithium-ion storage. Adv Energy Mater 2012;2:95–102.
[12] Virojanadara C, Watcharinyanon S, Zakharov AA, et al. Epitaxial graphene on 6H-SiC and Li intercalation. Phys Rev B 2010;82:2460–8.
[13] Lipson AL, Chattopadhyay S, Karmel HJ, et al. Enhanced lithiation of doped 6H silicon carbide (0001) via high temperature vacuum growth of epitaxial graphene. J Phys Chem C 2012;116:20949–57.
[14] Li H, Yu H, Zhang X, et al. Bowl-like 3C-SiC nanoshells encapsulated in hollow graphitic carbon spheres for high-rate lithium-ion batteries. Chem Mater 2016;28:1179–86.
[15] Shi Y, Zhang F, Hu Y, et al. Low-temperature pseudomorphic transformation of ordered hierarchical macro-mesoporous SiO_2/C nanocomposite to SiC via magnesiothermic reduction. J Am Chem Soc 2018;132:5552–3.
[16] Chen SP, Xing K, Wen M, et al. Hierarchical assembly and superior sodium storage properties of a sea-sponge structured C/SnS@C nanocomposite. J Mater Chem A 2018;6:7631–8.
[17] Chen SP, Wu QN, Wen M, et al. Sea-sponge-like structure of nano-Fe_3O_4 on skeleton-C with long cycle life under high rate for Li-ion batteries. ACS Appl Mater Interfaces 2018;10:19656–63.
[18] Stöber W, Fink A, Bohn E, et al. Controlled growth of monodisperse silica spheres in the micron size range. J Colloid Interface Sci 1968;26:62–9.
[19] Bao Z, Weatherspoon MR, Shian S, et al. Chemical reduction of three-dimensional silica micro-assemblies into microporous silicon replicas. Nature 2007;446:172–5.
[20] Richman EK, Kang CB, Brezesinski T, et al. Ordered mesoporous silicon through magnesium reduction of polymer templated silica thin films. Nano Lett 2008;8:3075–9.
[21] Ngo DT, Le HTT, Pham X, et al. Facile synthesis of Si@SiC composite as an anode material for lithium-ion batteries. ACS Appl Mater Interfaces 2017;9:32790–800.
[22] Wen Z, Lu G, Cui S, et al. Rational design of carbon network cross-linked Si–SiC hollow nanosphere as anode of lithium-ion batteries. Nanoscale 2014;6:342–51.
[23] Wang C, Li Y, Ostrikov KK, et al. Synthesis of SiC decorated carbonaceous nanorods and its hierarchical composites Si@SiC@C for high-performance lithium ion batteries. J Alloy Compd 2015;646:966–72.
[24] Ahn J, Kim HS, Pyo J, et al. Variation in crystalline phases: controlling the selectivity between silicon and silicon carbide via magnesiothermic reduction using silica/carbon composites. Chem Mater 2016;28:1526–36.
[25] Putz A, Putz M. Spectral inverse quantum (spectral-IQ) method for modeling mesoporous systems: application on silica films by FTIR. Int J Mol Sci 2012;13:15925–41.
[26] Zhuang H, Zhang L, Staedler T, et al. Nanoscale integration of SiC-SiO_2 core-shell nanocables in diamond through a simultaneous hybrid structure fabrication. Appl Phys Lett 2012;100:193102.
[27] Chen Z, Cao Y, Qian J, et al. Antimony-coated SiC nanoparticles as stable and high-capacity anode materials for Li-ion batteries. J Phys Chem C 2010;114:15196–201.
[28] Hu Y, Liu X, Zhang X, et al. Bead-curtain shaped SiC@SiO_2 core-shell nanowires with superior electrochemical properties for lithium-ion batteries. Electrochim Acta 2016;190:33–9.

[29] Sun XJ, Shao CZ, Zhang F, et al. SiC nanofibers as long-life lithium-ion battery anode materials. Front Chem 2018;6:166.
[30] Sun H, Xin G, Hu T, et al. High-rate lithiation-induced reactivation of mesoporous hollow spheres for long-lived lithium-ion batteries. Nat Commun 2014;5:4526.

Weina Li is currently a Master student in the School of Chemical Science and Engineering, Tongji University. Her research is focused on the synthesis of carbon-based nanomaterials for electrochemical energy storage.

Ming Wen is a full professor in the School of Chemical Science and Engineering at Tongji University. She received her Ph.D. degree in Analysis Chemistry in 2002 from Kinki University in Japan, and International Academic Communication in Tohoku University (Japan) and Humboldt-Universität zu Berlin (Germany) in 2011 and 2015, respectively. Her scientific interests are focused on metal & alloy catalytic nanomaterials for hydrogen generation, environments treatment, and electrodes nanomaterials.